IEEE Photonics Journal
An IEEE Photonics Society Publication

Open Access

Small-Signal Analysis of High-Performance VCSELs

Volume 11, Number 2, April 2019

Wissam Hamad, *Member, IEEE*
Marwan Bou Sanayeh, *Member, IEEE*
Tobias Siepelmeyer
Hassan Hamad
Werner H. E. Hofmann, *Member, IEEE*

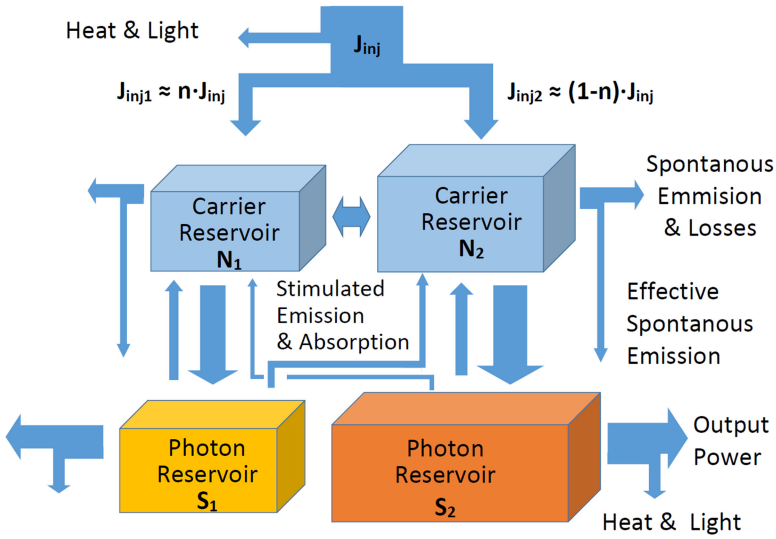

DOI: 10.1109/JPHOT.2019.2901722
1943-0655 © 2019 CCBY

Small-Signal Analysis of High-Performance VCSELs

Wissam Hamad,[1] ***Member, IEEE***,
Marwan Bou Sanayeh,[2] ***Member, IEEE***, **Tobias Siepelmeyer**,[1]
Hassan Hamad,[2] **and Werner H. E. Hofmann**,[1] ***Member, IEEE***

[1]Technische Universität Berlin, Institute of Solid State Physics and Center of Nanophotonics, Berlin 10623, Germany
[2]ECCE Department, Faculty of Engineering, Notre Dame University -Louaize 72, Zouk Mikael, Lebanon

DOI:10.1109/JPHOT.2019.2901722

Manuscript received December 13, 2018; accepted February 22, 2019. Date of publication February 26, 2019; date of current version March 14, 2019. This work was supported in part by the Erasmus+ programme and the German Research Foundation (DFG) within the Collaborative Research Center "Semiconductor Nanophotonics" (CRC 787) and the Open Access Publication Fund of TU Berlin. Corresponding author: Wissam Hamad (e-mail: w.hamad@tu-berlin.de).

Abstract: In this paper, a comprehensive model to describe the small-signal modulation response of ultra-high performance single- and multi-mode vertical-cavity surface-emitting lasers (VCSELs), with modulation bandwidths exceeding 30 GHz, is presented. Traditionally, utmost simplified dynamic models are used to extract dynamic figures of merit from single-mode edge-emitting lasers. These methods are later on also applied to evaluate the dynamic performance of VCSELs, even though these devices have a very different geometrical layout and modal confinement. However, to understand the dynamic performance of high-speed VCSELs, a model supporting the transverse and longitudinal mode profile, and the driving current inhomogeneity in the active region, is needed. Therefore, multi-mode VCSEL rate equations are established here. Moreover, to access the dynamic figures of merit of these devices, a comprehensive analytical fitting function based on our carrier reservoir splitting approach is derived. Thus, because of the high carrier and photon densities inside these optimized VCSELs, the common carrier reservoir splits up as a result of numerous effects such as mode competition, carrier diffusion and spatial hole burning. These and other effects have a tremendous impact on the small signal modulation response shape and bandwidth, and also on the current distribution profile in the carrier reservoirs. Compared with our recently reported work, this novel model presented includes the effects of gain compression and inhomogeneous current injection between the different lasing modes. Consequently, it is found that the further tuning of our multi-mode VCSEL dynamic model, to include these effects, yields a more physical and consistent figures of merit of high-performance VCSELs.

Index Terms: Carrier reservoir splitting, inhomogeneous current injection, multi-mode rate equations, mode competition, small-signal-modulation response, ultra-high performance VCSELs, and transfer function.

1. Introduction

Nowadays, vertical cavity surface-emitting lasers (VCSELs) have emerged as a ground-breaking solution for the increasing bandwidth demand of short reach optical links, where data rates $>$100 Gbit/s are required. Data rates in this range need directly modulated VCSELs with ultimate speed ratings towards the 40 GHz bandwidth level [1], [2]. Consequently, this motivated an intensive research

towards a deeper understanding of the device physics and dynamic performance. Furthermore, this frontier research and other aspects such as structural and process parameter optimization led to an improvement in the modulation performance of these semiconductor lasers, pushing them beyond the 30 GHz bandwidth limit [3]–[7]. In the meantime, and despite the intensive research conducted to understand the underlying physics behind the multi-mode behavior in oxide VCSELs and their impact on the intrinsic laser dynamics, many ambiguities still exist concerning the nature of the abnormal multi-peak phenomenon and the notches occurring in the small-signal modulation response of VCSELs. These multiple local maxima which appear in the transfer function signal of the multi-mode VCSELs, deviate substantially from the standard single-mode model normally applied to characterize these multimode devices. This aforementioned simple-mode model resembles a second order low pass filter. Moreover, the adapted single-mode fit model, which is based on this model, can only reproduce a single resonance peak and thus fails to fit the small-signal data accurately.

The small-signal modulation response of a VCSEL can be isolated from the entire system, thus providing accurate information on the intrinsic laser dynamics. Until now, it is assumed that the small-signal dynamic behavior of oxide-confined multi-mode (MM) VCSELs can be fully modelled using the single-mode (SM) rate equations developed for edge-emitters, even though the deviation between the SM based model and the measured data is substantially large. Moreover, VCSEL mode dynamics and thus the small-signal modulation response differ from these of longitudinal edge-emitting lasers due to the unique spatial interaction of the multiple transverse modes in MM-VCSELs. Another main aspect which should be taken into consideration is the inhomogeneity of the pumping current in the active region of VCSELs. In contrast to edge-emitters, VCSELs uses a ring form electrode to pump the lasing modes and oxide apertures for confining the driving current. This, and other nonlinear effects, leads to a huge inhomogeneity in the current density distribution along the lateral direction in the active region.

In fact, the dynamic behavior of MM-VCSELs can, to a certain extent, be modelled by the SM rate equations as long as the lasing modes share a common carrier reservoir, or the VCSEL is still lasing in the SM regime [7]. However, the shared carrier reservoir in ultra-high performance VCSELs driven at high optical densities tends to split up among the resonating modes, making the SM modulation approach fail to model the small-signal modulation behavior of these high-performance VCSELs. This splitting in the carrier reservoir occurs mainly because spatial hole burning (SHD) and other nonlinear effects such as mode competition, carrier diffusion.

In this work, our latest advanced MM interaction Matrix and our novel MM model are presented. The main concept of our promising approach is based on mode competition for the shared carrier reservoirs [8]–[10]. However, compared to our former reported derivations [7], our novel Multi-mode rate equations were further developed to include the effects of gain compression and inhomogeneous current injection distribution between the different lasing modes in the active region.

In our previous work [7], and due to the computational complexity as a result of the oversized MM interaction matrix, the reported model was simplified by assuming that the gain compression is negligible and the injection current density distribution is homogeneous across the active region. However, in actual high-performance VCSEL devices, gain compression and inhomogeneity in the injection current density can have a significant effect on the small signal dynamics, especially at high bias currents. Hence, the MM interaction matrix, which models the communication and coupling of different lasing modes among each other and with their underlying carrier reservoirs, is adapted to include these two important effects. This novel model is going to be discussed in details in this work. Moreover, a more comprehensive analytical transfer function for fitting the measured modulation response is also presented. This analytical function gives a deeper understanding of the device multi-mode laser dynamics and ensure also a better access to the nonlinear modal competition behavior for the carrier density in the active region for such high-performance VCSELs.

In this work, we show that inside our latest generation of VCSELs with highest carrier and photon densities, the common carrier reservoir splits up as a result of numerous effects such as mode competition, carrier diffusion and spatial hole burning (SHB). Analyzing the small-signal dynamics of VCSELs with the advanced model presented here, gives excellent fitting outcomes, especially

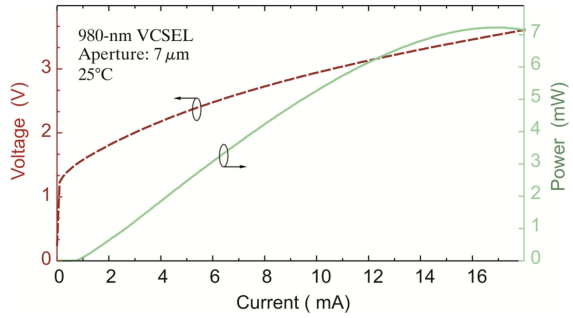

Fig. 1. L-I-V Characteristics of the oxide-confined 980-nm VCSEL at room temperature. The characterized VCSEL has an aperture diameter of ~7 μm.

compared to the over simplified SM model that is commonly used in literature. We are also seeing the dynamic figures of merit splitting up between the two lasing modes ensembles due to mode competition. Interestingly, such splitting up behavior was observed in the static L-I characteristics of VCSELs [14]. This detailed understanding of the VCSELs modulation response enables further optimization of these lasers for the next generation high-speed devices.

2. Device Structure and Advanced Small-Signal Model

First we are going to discuss the device structure and its static performance, and afterwards, the derivation of the novel MM small-signal model is presented.

2.1 VCSEL Device Layout and Static Performance

The small-signal analysis is performed on high-speed, temperature-stable 980 nm VCSELs. Sharing the very short half-wavelength cavity and a binary bottom-mirror with 32 pairs, the epitaxial layers, grown by IQE Europe, are further optimized in order to minimize internal losses. Parasitics are controlled by two oxide apertures and highly conducting current-spreading layers. InGaAs multiple quantum well active layers with strain compensated GaAsP barriers were utilized for getting a high differential gain. The 22-pair $Al_{12}Ga_{88}As/Al_{90}Ga_{10}As$ top-mirror was replaced by an 18-pair $GaAs/Al_{90}Ga_{10}As$ mirror to decrease photon lifetime, and to improve confinement and heat extraction.

The lasing *L-I-V* characteristics of the device are presented in Fig. 1. The 980-nm VCSEL features an aperture for current confinement of about 7 μm in diameter with a threshold current below 0.8 mA, and a differential slope of ~0.64 W/A at 25 °C (equaling a differential quantum efficiency of 50%). The maximum optical output power is above 7 mW, and the differential series resistance is 75 Ω.

2.2 Advanced Small-Signal Model

In order to derive the MM transfer functions, the model based on the standard SM rate equations was expanded to consider the coupling of two different mode ensembles through their lateral spatial distribution and overlap in the carrier reservoirs. If the modal competition for the carriers in the carrier reservoir is not included explicitly in the interaction matrix as two distinct carrier reservoir, it is not possible to obtain more than one resonance peak in the modulation response fit model. Thus, solving the resulting interaction matrix gives rise to a SM transfer function even if two or more modes are included. However, if the spatial distribution of the modal fields in the carrier reservoir is taken into consideration, and the carrier reservoirs are split up between the two mode ensembles, two resonance peaks can be fitted.

As this model was consistently expanded from the commonly used SM model, we also could easily expand well-known figures of merit such as the relaxation oscillation frequency

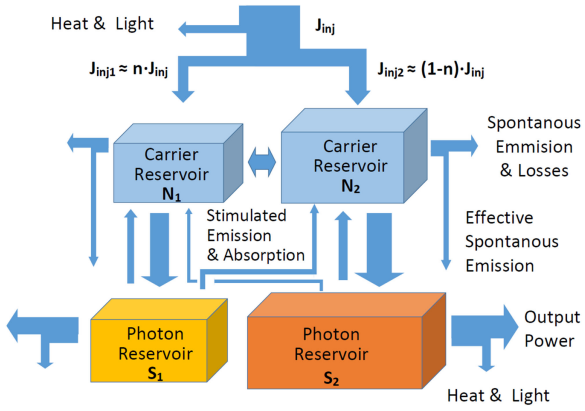

Fig. 2. Coupled Multiple-Reservoir Multi-Mode Model. In this Model the modes confine their independent carrier reservoirs. This split up behavior corresponds to spatial hole burning of multiple transverse mode ensembles of a VCSEL. A single drive current Jinj also splits up proportional to an inhomogeneity factor n. This model can explain the dynamic behavior of real-world high-speed VCSEL devices well.

and the damping factor. Our latest generation of VCSELs serve as sample-devices for detailed investigation. As already mentioned, this novel model also includes the effects of gain compression and inhomogeneity in the injection current distribution, effects that have a significant influence on the small signal dynamics.

In order to get a better insight on the derivation of the proposed advanced fitting model, we quickly review the different derivation steps leading to the system's small-signal modulation response. The first step is done by linearizing the system of differential equations representing the rates of change in both carrier and photon reservoir densities in the reservoir based model (see Fig. 2). Rewriting these linearized equations results in the rate coefficients shown in equations (1−4), where the subscript i refers to the i-th mode ensemble in the corresponding carrier or photon reservoirs,

$$\mu_{NiNi} = \delta J_{th_i}/\delta N_i + v_g a_i S_i \tag{1}$$

$$\mu_{NiSi} = v_g g_{th_i} - v_g a_{p_i} S_i \tag{2}$$

$$\mu_{SiNi} = \Gamma_i v_g a_i S_i \tag{3}$$

$$\mu_{SiSi} = \Gamma_i v_g a_{p_i} S_i \tag{4}$$

where g_i represents the optical material gain of the *i*-th mode under all operating conditions and g_{th_i} at threshold, a_i and a_{p_i} are the differential gain and the negative gain derivatives, respectively. Furthermore, N_i is the carrier density and S_i is the photon density in the active region and the optical cavity, respectively. Moreover, Γ_i is the confinement factor, v_g is the group velocity. Finally, the carrier recombination density due to spontaneous emission or losses is given by J_{th_i}.The equations (1−4) are derived for operating conditions well above lasing threshold.

The relaxation oscillation frequency ω_{Ri}, and the damping factor γ_i in terms of the simplified rate coefficients can be introduced as

$$\omega_{Ri}^2 = \mu_{NiNi}\mu_{SiSi} + \mu_{NiSi}\mu_{SiNi} \tag{5}$$

$$\gamma_i = \mu_{NiNi} + \mu_{SiSi} \tag{6}$$

As shown in different literature [7] and [12], the intrinsic modulation response for SM-VCSELs, $H_{SM}(\omega)$, is gives as

$$H_{SM}(\omega) = \frac{dP}{dI} = \frac{h\nu}{e}\eta_d v_g g_{th} \cdot \frac{\mu_{SN}}{\det \mathrm{M}_{sm}} = \frac{h\nu}{e}\eta_d \cdot \frac{{\omega_R}'^2}{\omega_R^2 + j\omega\gamma - \omega^2} \tag{7}$$

where η_d is the differential quantum efficiency and $\omega_R'^2 = v_g g_{th}\mu_{SN}$. The relaxation oscillation frequency ω_R usually replaces ${\omega_R}'$ for common physical device parameters [11]. This approximation is usually acceptable for the SM modulation approach, as it does not affect the shape of the modulation curve. However, at high driving currents care must be taken, especially, when carrier reservoir split-up is established. Using equations (1−6), and later replacing the carrier density by the total laser output power P, leads to the derivation of the theoretical intrinsic transfer function. This transfer function describes the small-signal modulation response of the laser to a driving sinusoidal injection current dI. It is worth mentioning that the aforementioned SM case represents the interaction of only one single lasing mode with its carrier reservoir and can be characterized by a 2 × 2 interaction matrix M_{sm} for SM-VCSELs.

Applying the MM rate equation analysis, a higher dimensional interaction matrix can be established for MM-VCSELs which is based on the rate coefficients developed for SM that is given in equations (1−4) along with the cross and coupling rate coefficients discussed later in equations (14−17). In this work, the system of differential equations for the multi-mode reservoir split-up model was adapted from [10]. For instance, a 4 × 4 matrix, which models the interaction and coupling of two lasing mode ensembles, is for most purposes sufficient to describe the intrinsic dynamics of MM-VCSELs. In general, these VCSELs are fabricated with a small circular aperture diameter, allowing only few modes to rise under operation. Hence, most of these transverse lasing modes are spatially localized in two main regions, and therefore can be grouped in the center and at the peripheral boundary of the carrier reservoir (mode ensemble). Therefore, the advanced MM transfer function can be derived using the 4 × 4 interaction matrix depicted in equation (8). However, expanding the number of carrier- and photon reservoirs to 2 and 2 reservoirs, respectively, induces the introduction of a second subscript character to the already existing ones. This step is essential in order to be able to distinguish the impact resulting from the different reservoirs on themselves and on one another. For example, μ_{N1S2} defines the impact on the first carrier reservoir N_1 caused by the changes in the second photon reservoir S_2. In obvious cases, this second subscript is omitted as in the single-mode, single-carrier reservoir case discussed previously.

It is important to mention at this stage that the rate coefficients (entries) of the MM interaction matrix depicted in equation (8) are still consistent with the single mode coefficients. However, particle conservation for carrier- and photon reservoir entities should be taken into consideration. For more details on the elaborate derivation steps please refer to [7].

$$\begin{pmatrix} j\omega + \mu_{N_1N_1} & \mu_{N_1N_2} & \mu_{N_1S_1} & \mu_{N_1S_2} \\ \mu_{N_2N_1} & j\omega + \mu_{N_2N_2} & \mu_{N_2S_1} & \mu_{N_2S_2} \\ -\mu_{S_1N_1} & 0 & j\omega + \mu_{S_1S_1} & 0 \\ 0 & -\mu_{S_2N_2} & 0 & j\omega + \mu_{S_2S_2} \end{pmatrix} \begin{pmatrix} dN_1 \\ dN_2 \\ dS_1 \\ dS_2 \end{pmatrix} = \begin{pmatrix} dJ_1 \\ dJ_2 \\ 0 \\ 0 \end{pmatrix} \equiv \mathbf{M} \cdot \mathbf{x} = \mathbf{i} \tag{8}$$

Solving the MM interaction matrix in equation (8) for the photon reservoir densities, and taking into consideration the boundary conditions imposed on the possible interactions, the MM modulation response can be derived. In order to maintain a compact representation of the MM modulation response, some practical figures of merits are going to be introduced.

Defining the photon lifetime τ_p in terms of α_{int} and α_m, which represent the internal and mirror losses, respectively,

$$\tau_p = \frac{1}{v_g(\alpha_{\mathrm{int}} + \alpha_m)} = \frac{1}{v_g \Gamma g_{th}}, \tag{9}$$

the determinant of the MM interaction matrix,det M, can be expressed in terms of the flowing figures of merit shown in equations (10−13), as $\det \mathrm{M} = \det \mathrm{M}_{m1} \cdot \det \mathrm{M}_{m2} - \Lambda_{m1,2} \cdot \Lambda_{m2,1}$,

$$\det \mathrm{M}_{m1} \equiv \omega_{R1}^2 + j\omega\gamma_1 - \omega^2 \tag{10}$$

$$\det \mathrm{M}_{m2} \equiv \omega_{R2}^2 + j\omega\gamma_2 - \omega^2 \tag{11}$$

$$\Lambda_{m1,2} \equiv s_{m1}\omega_{R2}^2(1 + j\omega\tau_p) \tag{12}$$

$$\Lambda_{m2,1} \equiv s_{m2}\omega_{R1}^2(1 + j\omega\tau_p) \tag{13}$$

where $\det \mathrm{M}_{mi}$ is written to resemble the single mode figure of merit $\det \mathrm{M}_{sm}$ (equation (7)). This is only done to maintain a compact and consistent representation of the final equations. Moreover, s_{m1} and s_{m2} represent the degree of spatial dependency of the two interacting carrier reservoirs with respect to the two different mode overlap volumes [10], therefore $\Lambda_{m1,2}$ and $\Lambda_{m2,1}$ can be considered as coupling factors which control the interaction between the two modes ensembles. In case where the two modes are not spatially overlapping, these factors will disappear and the resulting small-signal modulation response will reduce to the sum of two independent SM systems. The so called coupling rate coefficients μ_{N1N2} and μ_{N2N1}, representing the interaction between the two different carrier reservoir densities N_1 and N_2, are shown in equations (14) and (15). Moreover, the interaction coefficients that are needed to model the cross reabsorption are expressed in equations (16) and (17).

$$\mu_{N1N2} = v_g a_2 S_2 \cdot s_{m2} = \mu_{N2N2} \cdot s_{m2} - (\delta J_{th_2}/\delta N_i) \cdot s_{m2} \tag{14}$$

$$\mu_{N2N1} = v_g a_1 S_1 \cdot s_{m1} = \mu_{N1N1} \cdot s_{\mathrm{m1}} - (\delta J_{th_1}/\delta N_i) \cdot s_{m1} \tag{15}$$

$$\mu_{N1S2} = v_g g_{th(m2)} \cdot s_{m2} = \mu_{N2S2} \cdot s_{m2} \tag{16}$$

$$\mu_{N2S1} = v_g g_{th(m1)} \cdot s_{m1} = \mu_{N1S1} \cdot s_{m1} \tag{17}$$

The total photon density is then given by the sum of the photon densities in each mode. Thus $dS = dS_1 + dS_2$ can then be defined as

$$dS = \frac{dJ_1\mu_{S1N1}\left[\det \mathrm{M}_{m2} - \Lambda_{m1,2}\right] + dJ_2\mu_{S2N2}\left[\det \mathrm{M}_{m1} - \Lambda_{m2,1}\right]}{\det \mathrm{M}_{m1} \cdot \det \mathrm{M}_{m2} - \Lambda_{m1,2} \cdot \Lambda_{m2,1}} \tag{18}$$

where $dJ_i = \frac{\eta_i}{eV_{act}} dI_i$ represents the differential injection current density for each mode, η_i represents the injection efficiency and V_{act} is the active volume of the carrier reservoir. The total differential laser output power can then be determined using the steady-state solution as

$$\begin{aligned} dP &= dP_1 + dP_2 = h\nu\eta_{opt}v_g V_{res}(\alpha_{\mathrm{int}} + \alpha_m)dS \\ &= h\nu\eta_{opt}v_g V_{res}\Gamma g_{th} dS = h\nu\eta_{opt}v_g V_{act} g_{th} dS \end{aligned} \tag{19}$$

where dP_1 and dP_2 represent the differential output power for modes 1 and 2, respectively, the confinement factor is given by $\Gamma = \frac{V_{act}}{V_{res}}$, and V_{res} is the volume of the optical resonator.

Finally, the small-signal MM modulation response $H_{MM}(\omega) = \frac{dP_1 + dP_2}{dI}$ can be represented by equation (20) as

$$H_{MM}(\omega) = \frac{h\nu}{e}\eta_i\eta_{opt}v_g g_{th} \frac{\frac{dI_1}{dI}\mu_{S1N1}\left[\det \mathrm{M}_{m2} - \Lambda_{m1,2}\right] + \frac{dI_2}{dI}\mu_{S2N2}\left[\det \mathrm{M}_{m1} - \Lambda_{m2,1}\right]}{\det \mathrm{M}_{m1} \cdot \det \mathrm{M}_{m2} - \Lambda_{m1,2} \cdot \Lambda_{m2,1}} \tag{20}$$

where the differential current $dI = dI_1 + dI_2$ is the sum of two differential injection currents in each carrier reservoir of the two modes. If we consider $\frac{dI_1}{dI} = n$ and $\frac{dI_2}{dI} = 1 - n$, where n is the injection current inhomogeneity factor, i.e., n and $1 - n$ are the fractions of the injection current distribution in each carrier reservoir, and realizing that the differential quantum efficiency $\eta_d = \eta_i\eta_{opt}$, then $H_{MM}(\omega)$ can be rewritten as

$$H_{MM}(\omega) \simeq \frac{h\nu}{e}\eta_d \frac{n\,\omega_{R1}'^2\left[\det \mathrm{M}_{m2} - \Lambda_{m1,2}\right] + (1-n)\,\omega_{R2}'^2\left[\det \mathrm{M}_{m1} - \Lambda_{m2,1}\right]}{\det \mathrm{M}_{m1} \cdot \det \mathrm{M}_{m2} - \Lambda_{m1,2} \cdot \Lambda_{m2,1}} \tag{21}$$

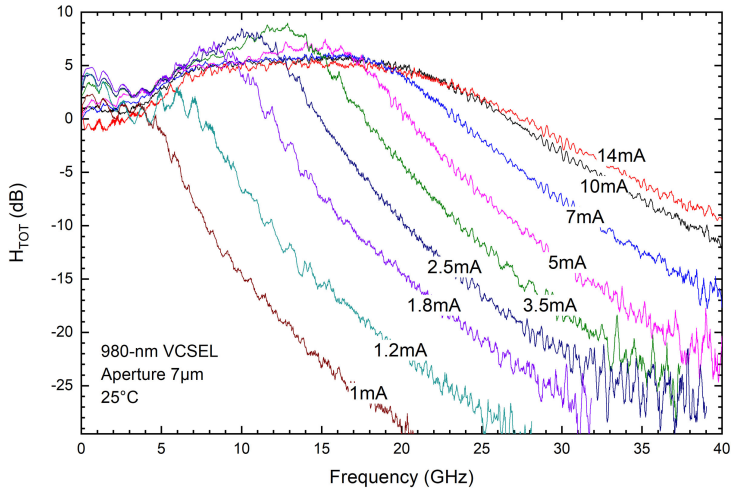

Fig. 3. Calibrated small-signal modulation response of a 980-nm MM and oxide-confined VCSEL with an aperture diameter of $\sim$7 μm. The curves depict the measured relative response data (S_{21}) for various driving currents at room temperature.

where $\omega'^2_{Ri} = v_g g_{th} \mu_{SiNi}$. The MM intrinsic modulation response shown in equation (21) is highly symmetrical and includes both gain compression and the inhomogeneous injection current distribution between the lasing modes in the VCSEL. As mentioned before, if the modes are not or negligibly spatially overlapping, i.e., $\Lambda_{m1,2} = \Lambda_{m2,1} \simeq 0$, then equation (21) will reduce to the weighted sum of two independent SM transfer function (equation (7)), however, still containing the injection current inhomogeneity factor n. This decoupled MM transfer function is then represented as

$$H_{MM-dec}(\omega) \simeq \underbrace{\frac{h\nu}{e}\eta_d \frac{n\,\omega'^2_{R1}}{\det \mathrm{M}_{m1}}}_{\text{mode1}} + \underbrace{\frac{h\nu}{e}\eta_d \frac{(1-n)\,\omega'^2_{R2}}{\det \mathrm{M}_{m2}}}_{\text{mode2}} \tag{22}$$

3. Figures of Merit and Device Performance

For modeling the total small-signal modulation response $H_{TOT}(\omega)$ of the VCSEL, the intrinsic transfer function $H_{MM}(\omega)$ is multiplied by the extrinsic transfer function of the parasitic network $H_{Par}(\omega)$. Traditionally, $H_{Par}(\omega)$ is modeled by a single parasitic pole [7]. However, we found that this approximation does not accurately represent the extrinsic behavior of VCSELs at high frequencies. Thus, for de-embedding the parasitic modulation response $H_{Par}(\omega)$ from $H_{TOT}(\omega)$, we developed an advanced transfer function, which is consistent with an elaborate analysis of advanced equivalent circuit modeling [13]. Equation (23) represents the total small-signal modulation.

$$H_{TOT}(\omega) = H_{MM}(\omega) \cdot H_{Par}(\omega) \tag{23}$$

3.1 DC-Offset and Injection Current Inhomogeneity

In logarithmic decibel scale, the total modulation response can be written as $H_{TOT}[dB] = 10\log_{10}|H_{TOT}(\omega)|^2$, which in fact is the S_{21} measured response given by the vector network analyzer (VNA). Figure 3 shows the calibrated small-signal modulation response of 980 nm MM oxide-confined VCSEL with an aperture diameter of $\sim$7 μm measured by a 40-GHz VNA (HP8722C). The curves describe the measured relative modulation response data (S_{21}) for various driving currents at room temperature. The modulation current is increased gradually up to 14 mA. Thermal rollover is reached at around 17 mA. The maximum 3-dB bandwidth of the device including chip-parasitics is found to exceed 32 GHz at 14 mA. The dc-offset appearing in Fig. 3 at $H_{TOT}(0)$ is

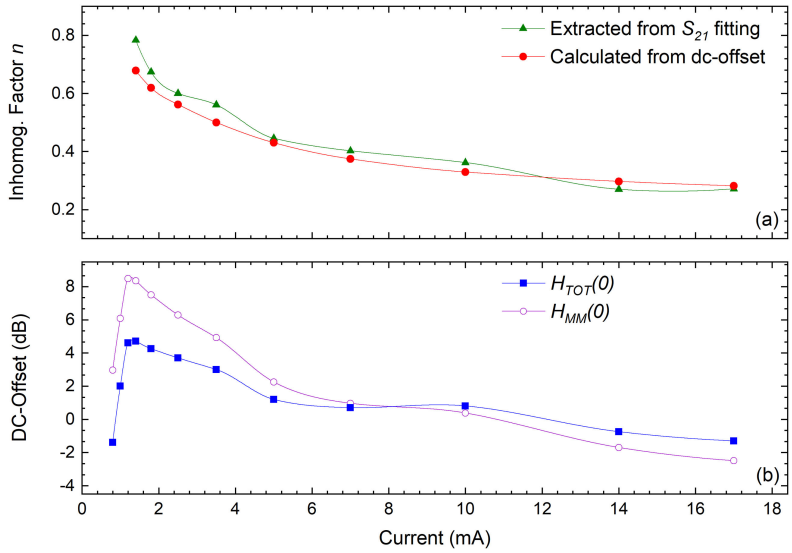

Fig. 4. (a) Injection current inhomogeneity factor n as a function of driving current extracted from fitting the S_{21} data using the advanced MM approach and calculated using equation (24). (b) DC-Offset at zero frequency before de-embedding parasitics ($H_{TOT}(0)$) and after de-embedding parasitics ($H_{MM}(0)$).

not artificially introduced to the plot. Looking back at the SM transfer function (equation (7)), and considering the approximation that $\omega_R' \approx \omega_R$, there will be no dc-offset in the modulation response at various driving currents, as $H_{SM}(0)$ is reduced to a constant. However, this outcome is not valid for the advanced MM approach, where $H_{MM}(0)$ is a function of the inhomogeneity factor n, which is directly related to the driving current. The relationship between the dc-offset and the inhomogeneity factor is shown in equation (24).

$$10\log_{10}\left|H_{MM}(0)\right|^2 = 10\log_{10}\left(\frac{n\,(1-s_{m1})+(1-n)\,(1-s_{m2})}{1-s_{m1}\cdot s_{m2}}\right)^2 \tag{24}$$

This current dependent dc-offset is commonly encountered in literature in the small-signal response measurements of MM-VCSELs, but has not been given much attention, even though it has been theoretically predicted while modeling spatial hole burning (SHB), carrier diffusion, and inhomogeneous injection effects in VCSELs [9].

Figure 4(a) shows the inhomogeneity factor *n* as a function of the injection current extracted from fitting the S_{21} data using the advanced MM approach, and compared to the calculated one using equation (24). Figure 4(b) depicts the dc-offset at very low frequency (near zero) before and after de-embedding parasitics. This parasitic free dc-offset $H_{MM}(0)$ is used in equation (24) to calculate the values of *n* shown in Fig. 4(a). As it can be seen from Fig. 4(a), the extracted and calculated values of *n* are highly matching, which confirms the potential of the MM model. Moreover, it can be seen that n decreases with increasing current. This means that at low driving currents, more carriers are being injected in the fundamental central modes, and as the current increases, more carriers will be transferred to the peripheral modes.

3.2 Consistent Expanded Figures of Merit

For further analysis and validation of the advanced MM model, equation (23) is used to fit the measured small-signal modulation response shown in Fig. 3, and extract consistent expanded figures of merit. Figure 5 shows selected small-signal modulation response curves at various driving currents. These has been chosen and artificially shifted along the y-axis for clarity. Moreover, the fitting done on these curves is performed using the advanced MM model. It can clearly be seen

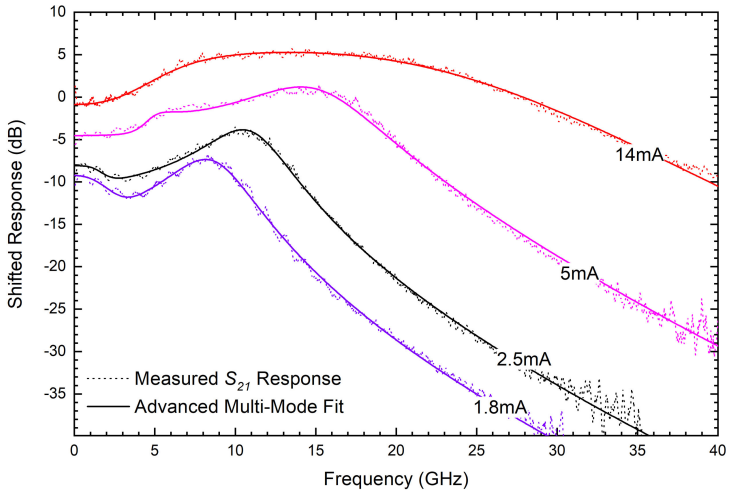

Fig. 5. Selected small-signal modulation response $H_{TOT}(f)$ curves at various driving currents and their advanced MM model fits. The curves are artificially shifted along the y-axis for clarity.

TABLE 1
Extracted figures of merit using the advanced fitting model at various injection currents

	1.8 mA	*2.5 mA*	*5 mA*	*14 mA*
$\omega_{R1} = 2\pi f_{R1}$ [s^{-1}]	35.2	56.9	84.7	79.9
$\omega_{R2} = 2\pi f_{R2}$ [s^{-1}]	38.6	49	59.4	142.1
γ_1 [s^{-1}]	43.6	21.4	50.1	59.2
γ_2 [s^{-1}]	25.2	31.7	15.9	187.2
n	0.78	0.61	0.44	0.27

that the fits match the measured data to a very high accuracy in all frequency and current ranges. Furthermore, it is obvious that this advanced model gives a much better representation and insight on the small-signal dynamics of high-speed VCSELs compared to the simple SM model which is commonly used for such analysis. Table 1 shows the extracted figures of merit ω_{R1}, ω_{R2}, γ_1, and γ_2 at various injection currents, along with the inhomogeneity factor n. The parameters $s_{m1} = 0.67$, $s_{m2} = 0.94$, and the photon lifetime $\tau_p = 3$ ps are calculated from physical device properties, and set as fixed values in the fitting equation. For example, the values for the mode overlap volumes s_{m1} and s_{m2} are calculated under the assumption that the VCSEL is lasing in the multimode regime with two mode ensembles, LP01 and LP11. The Photon life time is estimated from the structural configuration which take into consideration the effective length L_{eff} and the inner cavity length L of the optical resonator along with the reduced intensity reflection coefficient R_t of the 22-pair top VCSEL mirror.

To get a deeper insight into the device physics and laser dynamics, the figures of merit extracted using equation (23) can be related and directly compared to that of the SM model to establish the consistently expanded D-factors and K-factors for the MM approach. Thus, the SM device

performance indicators are defined using equations (5–6) as

$$\begin{aligned}\gamma = \mu_{NN} + \mu_{SS} &= v_g a S + \Gamma v_g a_p S + \underbrace{\frac{\delta}{\delta N} J_{th} + J_{sp}\frac{\Gamma}{S}}_{\equiv \gamma_o} \\ &= \overbrace{v_g a S \cdot v_g(\alpha_i + \alpha_m)}^{\omega_R^2} \cdot \underbrace{\frac{1 + \Gamma a_p / a}{v_g(\alpha_i + \alpha_m)}}_{\equiv K/4\pi^2} + \gamma_0 \\ &= f_R^2 \cdot K + \gamma_0\end{aligned} \tag{25}$$

for the damping rate γ. The relaxation oscillation frequency ω_R is given by

$$f_R \equiv D\sqrt{I - I_{th}}$$

where

$$D = \frac{1}{2\pi}\sqrt{\frac{v_g \eta_i a}{e V_{res}}} \tag{26}$$

with V_{res} as the volume of the optical resonator.

Consistently expanding these SM figures of merits, we can define performance indicators for the total emission as well as for each independent mode ensemble alone as

$$\sum \gamma_i = K_{TOT} \sum f_{Ri}^2 + \gamma_0 \tag{27}$$

$$\sqrt{\sum f_{Ri}^2} = D_{TOT}\sqrt{I - I_{th}} \tag{28}$$

where f_R is relaxation oscillation frequency, K_{TOT} and D_{TOT} are the K- and D-factors of the total laser emission, respectively, and γ_0 is the damping offset of the total emission. For each mode ensemble (central or peripheral modes), equations (28) and (28) can be adapted to calculate the corresponding individual K- and D- factors, K_i and D_i, as $\gamma_i = K_i \sum f_{Ri}^2 + \gamma_{0i}$, and $f_{Ri} = D_i\sqrt{I - I_{th}}$, respectively.

Figure 6(a) shows the damping rates vs. the sum of the squared relaxation oscillation frequencies for the total, central, and peripheral modes emissions. Figure 6(b) depicts the relaxation oscillation frequencies vs. the square root of the total injection current above threshold for the total and each mode ensemble emissions.

Interestingly, the total emission properties are almost linearly increasing, even though the individual modes exhibit an unsteady behavior, which is probably the result of mode competition and switching, due to SHB and thermal lensing, as the current increases. These properties has also been theoretically predicted by simulations for mode resolved power–current characteristics of oxide-confined VCSELs [14]. Form the slopes of the total emission curves, the total K- and D- factors can be extracted, leading to the values of $K_{TOT} = 0.38$ ns and $D_{TOT} = 7.56$ GHz/$\sqrt{\text{mA}}$.

4. Conclusion

In conclusion, we developed a comprehensive model to describe the small-signal modulation response of ultra-high performance VCSELs. Furthermore, our novel Multi-mode rate equations, include the effects of gain compression and inhomogeneous current injection between the different lasing modes. Moreover, an analytical fitting function for the modulation response, which is based on our carrier reservoir splitting approach, was derived. This analytical fitting function allows the extraction of consistently expanded figures of merit and performance indicators for these devices. This gives a deeper understanding of the device multi-mode laser dynamics and give a better access to the nonlinear modal competition behavior for the carrier density in the active region for such high-performance VCSELs. Consequently it was found that inside our latest generation of VCSELs

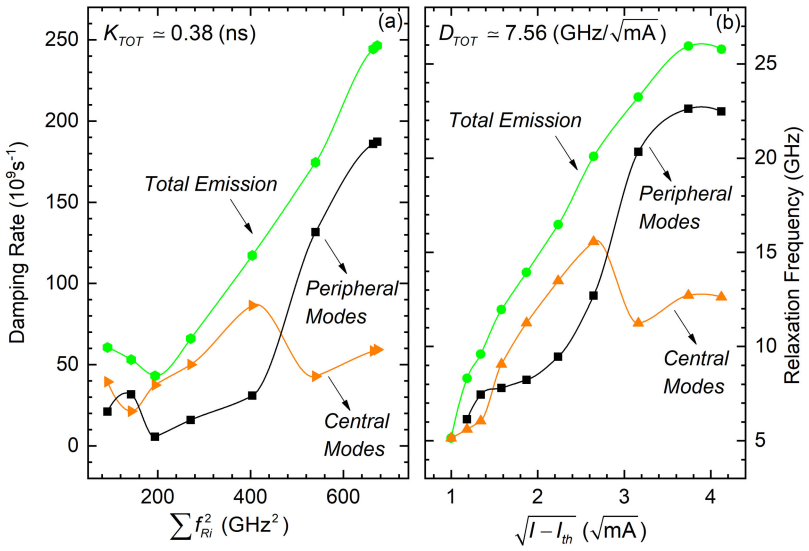

Fig. 6. (a) Damping rates vs. the sum of the squared relaxation oscillation frequencies for the total, central, and peripheral modes emissions. (b) Relaxation oscillation frequencies vs. the square root of the total injection current above threshold for the total and each mode ensemble emissions. The dynamic behavior splits up by mode competition like the static LI characteristics.

with highest carrier and photon densities, the common carrier reservoir splits up as a result of numerous effects such as mode competition, carrier diffusion and spatial hole burning (SHB). Analyzing the small-signal dynamics of VCSELs with the advanced model presented here, excellent fitting outcomes, especially compared to the over simplified SM model that is commonly used in literature could be achieved. We are seeing the dynamic figures of merit splitting up due to mode competition like the static LI characteristics. This detailed understanding of the VCSELs modulation response enables further optimization of these lasers for the next generation high-speed devices.

Acknowledgment

The authors would like to thank the German Research Foundation and the Open Access Publication Funds of TU Berlin.

References

[1] D. M. Kuchta *et al.*, "A 71-Gb/s NRZ modulated 850-nm VCSEL-based optical link," *IEEE Photon. Technol. Lett.*, vol. 27, no. 6, pp. 577–580, Mar. 2015.
[2] W. Hofmann and D. Bimberg, "VCSEL-based light sources-scalability challenges for VCSEL-based multi-100-Gb/s systems," *IEEE Photon. J*, vol. 4, no. 5, pp. 1831–1843, Oct. 2012.
[3] K. Szczerba, P. Westbergh, M. Karlsson, P. A. Andrekson, and A. Larsson, "70 Gbps 4-PAM and 56 Gbps 8-PAM using an 850 nm VCSEL," *J. Lightw. Technol.*, vol. 33, no. 7, pp. 1395–1401, Apr. 1, 2015.
[4] J. A. Tatum *et al.*, "VCSEL-based interconnects for current and future data centers," *J. Lightw. Technol.*, vol. 33, no. 4, pp. 727–732, Feb.15, 2015.
[5] H. Hatakeyama *et al.*, "Highly reliable high-speed 1.1-μm-range VCSELs with InGaAs/GaAsP-MQWs," *IEEE J. Quantum Electron.*, vol. 46, no. 6, pp. 890–897, Jun. 2010.
[6] E. Haglund *et al.*, "30 GHz bandwidth 850 nm VCSEL with sub-100 fJ/bit energy dissipation at 25-50 Gbit/s," *Electron. Lett.*, vol. 51, no. 14, pp. 1096–1098, 2015.
[7] W. Hamad, S. Wanckel, and W. H. E. Hofmann, "Small-signal analysis of ultra-high-speed multi-mode VCSELs," *IEEE J. Quantum Electron.*, vol. 52, no. 7, pp. 1–11, Jul. 2016, Art. no. 2400311.
[8] M. S. Torre and H. F. Ranea-Sandoval, "Modulation response of multiple transverse modes in vertical-cavity surface-emitting lasers," *IEEE J. Quantum Electron.*, vol. 36, no. 1, pp. 112–117, Jan. 2000.
[9] R. Schatz and M. Peeters, "Modeling spatial hole burning and mode competition in index-guided VCSELs," in *Proc. SPIE*, Apr. 2003, vol. 4942, pp. 158–169.

[10] A. Valle and L. Pesquera, "Theoretical calculation of relative intensity noise of multimode vertical-cavity surface-emitting lasers," *IEEE J. Quantum Electron.*, vol. 40, no. 6, pp. 597–606, Jun. 2004.
[11] L. A. Coldren, S. W. Corzine, and M. L. Mashanovitch, "Dynamic Effects," *Diode Lasers and Photonic Integrated Circuits*. 2nd ed. Hoboken, NJ, USA: Wiley, 2012.
[12] W. Hofmann, "InP-based long-wavelength VCSELs and VCSEL arrays for high-speed optical communication," in *Proc. Sel. Topics Semicond. Phys. Technol.*, pp. 25–40, 2009.
[13] W. Hamad *et al.*, "Modulation response, impedance, and equivalent circuit of ultra-high-speed multi-mode VCSELs," in *Proc. SPIE*, 2018, vol. 10812, Art. no. 1081203.
[14] J. S. Gustavsson, J. A. Vukusic, J. Bengtsson, and A. Larsson, "A comprehensive model for the modal dynamics of vertical-cavity surface-emitting lasers," *IEEE J. Quantum Electron.*, vol. 38, no. 2, pp. 203–212, Feb. 2002.